The Near-Tip Fields of Fast Cracks

Ariel Livne, *et al.*

Science **327**, 1359 (2010);
DOI: 10.1126/science.1180476

modified parameters (*7*) to account for the present experimental conditions. Our choice of parameters reflects the reduced amount of TGA per CdTe, resulting in a net decrease of the charge, an increase of the face-face attraction energy, and a change in the direction of the dipole moment as compared with the conditions under which chains are obtained.

We used a recently developed technique for predicting ordered assemblies of building blocks with strong interactions via bottom-up building block assembly (BUBBA) (*26*) to determine the preferred local packing structure of tetrahedrons within ribbons. Then, Monte Carlo simulations were used to calculate the energy as a function of ribbon width to ascertain whether, and under what conditions, ribbons of finite width (rather than chains or sheets) (*1*, *8*) were the minimum energy structures. We found that NPs form four interdigitated layers grouped in two bilayers with tetrahedrons arranged hexagonally and inverted in alternate layers for denser packing (Fig. 4), which is consistent with TEM and SEM observations (Figs. 1, G to I, and 2B), albeit without the packing perfection seen in the simulations. The energy of the ribbon is minimized for a range of widths of ~18 to 110 nm, which matches structural parameters of TRs very well (Figs. 1 to 3). Increasing the charge resulted in more narrow ribbons, whereas decreasing the charge resulted in wider ribbons.

Overall, the multiparticle behavior and transition from packing into chains, ribbons, and sheets can be understood in terms of a competition between the face-face attraction and the charge-charge repulsion. For low charge and strong face attraction, as was the case in previous studies (*1*), particles pack very densely and would, if constrained to the same packing structure, form infinite two-dimensional sheets. By increasing the amount of charge, an infinite sheet becomes energetically unfavorable because of the long-range electrostatic repulsion, and NPs assemble as ribbons. Further increase of particle charge will eventually result in chains, as was observed for higher concentrations of TGA (*6*, *8*). Note that this concerns the effect of NP charge before the assembly. Once a larger NP system is assembled and held together by strong interparticle interactions, it may not be able to transition freely from sheets to ribbons of smaller width and then to chains. However, if there are structural units more loosely attached to each other, such as ribbons in bunches, they do separate, as can be seen by the unraveling of the bouquets of TRs (Fig. 3D and fig. S14).

The notion of evolving NP assemblies and better understanding of parameters controlling behavior of large numbers of nanoscale particles as a whole will be useful for many other nanocolloid systems. This study demonstrates that light can induce microscale twisting of the matter due to strong effect on the mutual interactions of nanoscale building blocks in a multibody system. The modulation in the pitch length for the TRs under different light intensities creates a new approach in the synthesis of nanostructures and new opportunities to generate nanomaterials with controlled circular dichroism and other optical, electronic, and mechanical properties.

References and Notes

1. Z. Tang, Z. Zhang, Y. Wang, S. C. Glotzer, N. A. Kotov, *Science* **314**, 274 (2006).
2. R. S. Yang, Z. L. Wang, *J. Am. Chem. Soc.* **128**, 1466 (2006).
3. S. C. Glotzer, M. J. Solomon, N. A. Kotov, *AIChE J.* **50**, 2978 (2004).
4. S. C. Glotzer, M. J. Solomon, *Nat. Mater.* **6**, 557 (2007).
5. C. Li, N. Murase, *Chem. Lett.* **34**, 92 (2005).
6. Z. Tang, N. A. Kotov, M. Giersig, *Science* **297**, 237 (2002).
7. See supporting material on *Science* Online.
8. Z. Zhang, Z. Tang, N. A. Kotov, S. C. Glotzer, *Nano Lett.* **7**, 1670 (2007).
9. W. W. Yu, L. H. Qu, W. Z. Guo, X. G. Peng, *Chem. Mater.* **15**, 2854 (2003).
10. J. Guo, W. Yang, C. Wang, *J. Phys. Chem. B* **109**, 17467 (2005).
11. K. V. K. Rao, S. V. N. Naidu, L. Iyengar, *J. Am. Ceram. Soc.* **51**, 467 (1968).
12. M. T. S. Nair, P. K. Nair, R. A. Zingaro, E. A. Meyers, *J. Appl. Phys.* **75**, 1557 (1994).
13. S. Busch *et al.*, *Eur. J. Inorg. Chem.* **1999**, 1643 (1999).
14. M. J. Bierman, Y. K. A. Lau, A. V. Kvit, A. L. Schmitt, S. Jin, *Science* **320**, 1060 (2008); published online 1 May 2008 (10.1126/science.1157131).
15. Y. Zhou, Q. M. Ji, M. Masuda, S. Kamiya, T. Shimizu, *Chem. Mater.* **18**, 403 (2006).
16. T. Vossmeyer *et al.*, *Science* **267**, 1476 (1995).
17. K. S. Cho, D. V. Talapin, W. Gaschler, C. B. Murray, *J. Am. Chem. Soc.* **127**, 7140 (2005).
18. L. S. Li, H. Z. Jiang, B. W. Messmore, S. R. Bull, S. I. Stupp, *Angew. Chem. Int. Ed.* **46**, 5873 (2007).
19. D. V. Talapin, H. Yu, E. V. Shevchenko, A. Lobo, C. B. Murray, *J. Phys. Chem. C* **111**, 14049 (2007).
20. X. D. Han *et al.*, *Nano Lett.* **7**, 452 (2007).
21. Y. Wang, Z. Tang, M. A. Correa-Duarte, L. M. Liz-Marzán, N. A. Kotov, *J. Am. Chem. Soc.* **125**, 2830 (2003).
22. T. McMillen, A. Goriely, *J. Nonlinear Sci. E* **12**, 241 (2002).
23. M.-F. Yu *et al.*, *Phys. Rev. B* **64**, 241403 (2001).
24. S. Yang *et al.*, *J. Am. Chem. Soc.* **128**, 10460 (2006).
25. A. Goriely, P. Shipman, *Phys. Rev. E* **61**, 4508 (2000).
26. E. Jankowski, S. C. Glotzer, *J. Chem. Phys.* **131**, 104104 (2009).

27. We acknowledge joint financial support by the Air Force Office of Scientific Research under Multiuniversity Research Initiative grant FA9550-06-1-0337. P.P. thanks the Fannie and John Hertz Foundation for support of his work through a graduate fellowship. This research was supported by the World Class University program through the Korea Science and Engineering Foundation funded by the Ministry of Education, Science and Technology (grant R33-2008-000-10021-0). We thank J. Kim (Univ. of Michigan) for helpful suggestions and discussions and W. Chen (JiangNan University) for assistance with some TEM data. P.P.'s work at the Center for Nanoscale Materials was supported by the Office of Science, Office of Basic Energy Sciences, of the U.S. Department of Energy under contract no. DE-AC02-06CH11357. P.P. acknowledges the support of the Willard Frank Libby postdoctoral fellowship from Argonne National Laboratory. The transmission electron microscope used in the study was supported by NSF grant DMR-9871177, and the scanning electron microscope used was supported by NSF grant DMR-0320740. S.C.G. and A.S. acknowledge the support of the J. S. McDonnell Foundation for the development of BUBBA. K.C. thanks Marie Curie Actions MOIF-CT-2006-039636 for financial support.

Supporting Online Material

www.sciencemag.org/cgi/content/full/science.1177218/DC1
Materials and Methods
SOM Text
Figs. S1 to S22
References

3 June 2009; accepted 2 February 2010
Published online 11 February 2010;
10.1126/science.1177218
Include this information when citing this paper.

The Near-Tip Fields of Fast Cracks

Ariel Livne, Eran Bouchbinder,* Ilya Svetlizky, Jay Fineberg†

In a stressed body, crack propagation is the main vehicle for material failure. Cracks create large stress amplification at their tips, leading to large material deformation. The material response within this highly deformed region will determine its mode of failure. Despite its great importance, we have only a limited knowledge of the structure of this region, because it is generally experimentally intractable. By using a brittle neo-Hookean material, we overcame this barrier and performed direct and precise measurements of the near-tip structure of rapid cracks. These experiments reveal a hierarchy of linear and nonlinear elastic zones through which energy is transported before being dissipated at a crack's tip. This result provides a comprehensive picture of how remotely applied forces drive material failure in the most fundamental of fracture states: straight, rapidly moving cracks.

Material failure occurs at small scales in the immediate vicinity of the tip of a crack. The existence of a crack in an otherwise perfect material dramatically amplifies applied stresses to values that approach a mathematical singularity at the crack's tip (*1*). The stress fields formed by a crack transport remotely applied elastic energy to the crack's tip, where the energy is dissipated by material fracture. Even small external stresses can generate sufficiently large stresses within this small microscopic region to initiate fracture. Linear elastic fracture mechanics (LEFM) provides the theoretical framework for understanding this stress amplification. LEFM assumes that the material under stress obeys linear elasticity (that is, Hooke's law) at every point up to the very near vicinity of a crack's tip. All of the complex dissipative and nonlinear processes that are involved in fracture and not described by LEFM are assumed to occur within a sufficiently small region around the tip. Nevertheless, this

Racah Institute of Physics, Hebrew University of Jerusalem, Jerusalem 91904, Israel.

*Present address: Department of Chemical Physics, Weizmann Institute of Science, Rehovot 76100, Israel.
†To whom correspondence should be addressed. E-mail: jay@vms.huji.ac.il

theory is very successful in describing the motion of a single straight crack in brittle materials (*2*).

Material failure, however, does not always occur via the propagation of individual straight cracks; propagating cracks are known to either microscopically branch or spontaneously oscillate if their propagation speed is sufficiently rapid (*3*, *4*). Moreover, how stresses are distributed and regularized near a crack's tip will determine the mode of failure (for example, brittle or ductile) and may hold the key to resolving important open questions about issues such as crack stability and path selection. Thus, the key to understanding these effects may lie in the structure of the near-tip region (*5*, *6*), where strains become so large that the linear stress-strain response underpinning LEFM must break down.

Progress in understanding the structure of this critical region has been, on the whole, limited by our lack of hard data describing the detailed physical processes that occur within. Due to the microscopic size and near–sound speed velocity of the near-tip region, direct measurements are very difficult, with numeric or atomistic calculations being the only means to assess it (*7*–*9*). As a result, attempts to understand the near-tip region have been largely empirical (*10*–*23*), using a wide variety of approaches. Many of these approaches assume that the material response is linearly elastic down to the immediate vicinity of the crack tip, where energy is dissipated. However, because of the large strains that always exist near a crack's tip, nonlinear elastic contributions must occur.

We studied the near-tip structure by using polyacrylamide gels (*24*). Their measured elastic response (up to strains of ~100%) is neo-Hookean (*24*), which is an extension of Hooke's law to large deformations (*25*). This constitutive relation has a well-founded statistical thermodynamic origin and is inherently nonlinear at large strains (*26*). These brittle materials provide a means to directly observe the detailed dynamics of rapid fracture, by slowing crack propagation velocities by nearly three orders of magnitude (typical crack speeds of 1200 m/s in glass correspond to 2 m/s in gels). Experiments have demonstrated that the dynamics of tensile cracks propagating in these gels are identical to those of other amorphous brittle materials (*27*). These include both single-crack dynamics (*1*, *28*) and crack instabilities (*3*, *27*) that occur at high propagation velocities v. Here, only single-crack modes for $v < 0.9c_S$ (where c_S is the shear wave speed) are considered, because crack instabilities were suppressed (*4*).

We studied the structure of the deformation fields of dynamic cracks at scales ranging from the system size (Fig. 1A) to those well within the region where nonlinear elasticity becomes important. We do this by tracking a passive tracer field imprinted on the gel faces with a fast high-resolution camera (Fig. 1B) (*24*). Comparison of each photograph with the undeformed tracer field provides the full displacement field, $\mathbf{u}(\mathbf{r}, t)$, surrounding the crack tip (Fig. 2A, inset), where $\mathbf{r}$ is the distance from the tip and t is time. Differentiation of $\mathbf{u}(\mathbf{r}, t)$ yields the strain fields (for example, Fig. 1B), so this method provides a precise measurement of all of the fields that locally drive a moving crack.

Crack advance is understood as a balance between the energy influx from the surrounding elastic fields and the energy dissipated at the crack's tip (fracture energy). In brittle materials, all dissipative processes occur near a crack's tip and include plastic deformation and bond breaking. The extent of the dissipative region may be determined by considering the energy flux through different contours surrounding the crack tip (Fig. 2A). At all scales beyond the dissipative region, the driving energy flux should be constant for steady-state propagation. The rate of energy per unit of sample width flowing through any closed contour, C, surrounding the crack tip is provided by the J integral (*1*)

$$J = \int_C [(U + \tfrac{1}{2}\rho \partial_t u_i \partial_t u_i) v n_x + s_{ij} n_j \partial_t u_i] dC \quad (1)$$

Here, $\mathbf{n}$ is an outward unit vector on C, ρ is the density of the undeformed material, U is a functional describing the material's elastic energy per unit of undeformed volume. For the incompressible neo-Hookean material described here, $U = \mu/2\,[F_{ij}F_{ij} + \det(\mathbf{F})^{-2} - 3]$, where μ is the shear modulus and $F_{ij} \equiv \delta_{ij} + \partial_j u_i$ (*29*). The stress tensor $s_{ij} = \partial_{Fij} U$ defines the material's constitutive law, where i and j run over the crack propagation direction x and the loading direction y in the undeformed (two-dimensional) frame. Their counterparts are x' and y' in the deformed (laboratory) frame. We consider steady-state propagation, so $\partial_t = -v\partial_x$ in Eq. 1. Under these conditions, the J integral is independent of the contour C if no dissipative regions (other than the immediate crack-tip region) are enclosed within.

The energy flux $G = J/v$ is the amount of energy flowing into C per unit of crack extension. Using the measured deformation field, G was computed for different contours about dynamic crack tips, with the encompassed area ranging from ~100 mm^2 down to ~500 μm^2 (Fig. 2A). At all measured scales, the energy flux computed for the neo-Hookean constitutive law is constant (Fig. 2A). This explicit demonstration of the path independence of the J integral has several important implications. Foremost, no bulk dissipation is observed down to the smallest measured contour, ~500 μm^2, implying a purely elastic response (that is, no irreversible deformation) on these scales. Furthermore, the constant G implies that the neo-Hookean description of the gels' elasticity, which is inferred from large-scale measurements and moderate strains, holds up in the

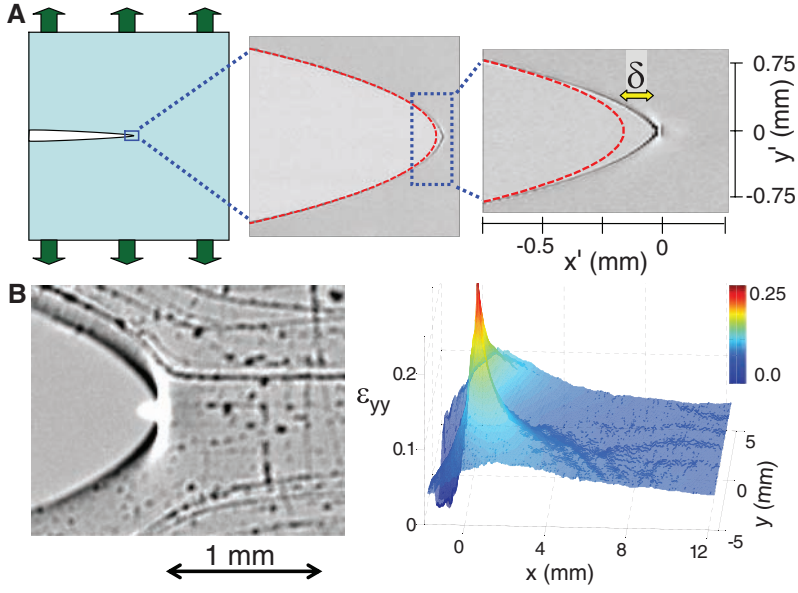

Fig. 1. (**A**) The tip [at $(x',y') = 0$] of a rapidly moving tensile crack ($v = 0.7c_S$) as seen at different scales. (Left) A schematic representation of the crack at the system size. (Center) A photograph of the crack's tip at a 5.2 × 5.4–mm scale demonstrating that its shape is close to the characteristic parabolic shape (dashed line) predicted by LEFM. (Right) A closeup of the same crack shows deviations from the parabolic crack-tip opening profile as the crack's tip is approached. The scale of this deviation is characterized by δ, the distance between the true crack tip and the tip location predicted by LEFM. (x',y') are the coordinates in the laboratory (deformed) frame, whereas (x,y) are the coordinates in the reference (undeformed) frame. (**B**) (Left) Blowup of the near-tip region of a different crack ($v = 0.48c_S$) with a tracer field imprinted on the gel (*24*). The displacement field $\mathbf{u} = (u_x,u_y)$ about the moving crack is found by comparing the tracer locations to their reference (pre-crack) state. (Right) The strain field, $\varepsilon_{yy} = \partial_y u_y$, up to 200 μm from the crack tip, is found by differentiating the measured displacement field. ε_{yy} diverges as the tip (located at the origin) is approached. The extreme strains in this region give rise to thickness variations, manifested by the lensing observed in the white region at the crack's tip (left).

near-vicinity of a crack tip, where extreme stresses prevail and the constitutive law cannot be directly measured.

Were we to assume a linear elastic material response, we would not find G to be constant, as demonstrated in Fig. 2A. Under these conditions, G converges asymptotically to the neo-Hookean value at large scales but deviates strongly as we approach the crack tip. Thus, although results derived from LEFM are correct for scales far enough from the crack tip (where strains are roughly <0.1), Fig. 2A shows that nonlinear elasticity becomes important as the crack tip is approached.

Are the values of G provided by Eq. 1 correct? By incorporating quadratic contributions to the stress-strain relation (*5*, *30*), a weakly nonlinear theory was recently derived that extended LEFM to strains of approximately 0.1 to 0.2. Whereas LEFM predicts singular strains of the form $r^{-1/2}$ in the near-tip vicinity (where r is the distance from the crack tip), this weakly nonlinear theory predicts additional strain contributions proportional to r^{-1} and displacement contributions proportional to $\log(r)$. At relatively large values of r, but still in regions where the strains are large enough to invalidate LEFM, this theory shows that a crack's tip has the same parabolic form (demonstrated in Fig. 1A) that is predicted by LEFM (*1*, *5*). The curvature of these parabolas provides an independent way to measure G (*1*, *28*). The comparison of this result in Fig. 2B with the J integral calculation, using neo-Hookean elasticity, indeed shows that the measurements are practically identical over the wide velocity range studied. This agreement is wholly nontrivial, because it results from entirely different measured inputs.

Just as the linear elastic description gives way to the weakly nonlinear description of fracture dynamics, the latter theory must, itself, break down at the smaller scales where even larger strains occur. This is demonstrated in Fig. 1A, right, where the far-field crack-tip profile breaks down as the crack tip is approached, and large discrepancies from its parabolic form are revealed. This breakdown has been characterized (*28*) by a velocity-dependent scale $\delta(v)$, defined as the distance from the measured crack tip to the one predicted by LEFM (Fig. 1A, right). For $r < \delta(v)$, strong elastic nonlinearities become increasingly important. We denote this region, where higher–than–second-order corrections to the stress-strain relations are needed, as "strongly nonlinear." Within this region, where strains are ~0.2 to 1, a perturbative approach is of limited applicability. Moreover, direct measurements of bulk deformation are, in general, difficult. The crack-tip profile, however, can be measured to even smaller scales.

The theoretical study of large deformations of neo-Hookean materials very close to the crack tip has a rich history (*29*, *31*–*34*). This work has yielded a solution for the deformation field asymptotically near a rapidly moving crack tip of the form (*33*)

$$u_y(r,\theta) = a(v)\, m(\theta;v)\, r^{1/2},$$
$$u_x(r,\theta) = [b(v) - 1]\cos(\theta)\, r \qquad (2)$$

where the function $m(\theta;v)$ is provided in (*24*) and a and b are velocity-dependent coefficients.

Equation 2 predicts an $r^{-1/2}$ variation of the strain $\partial_y u_y$, similar to the linear elastic prediction, but at much smaller scales. Thus, the crack-tip profile is parabolic in this limit, with the velocity-dependent curvature $b(v)/a^2(v)$ presented in Fig. 3. Figure 3A demonstrates that this parabolic profile differs significantly from the one at large scales (see also Fig. 1A). Such parabolic profiles, at comparable scales, are also observed in finite element calculations for static cracks in neo-Hookean materials (*35*).

Although the parabolic crack-tip profile, which is observed within the highly nonlinear region, is consistent with the asymptotic solution given in Eq. 2, one can imagine that any crack-tip profile that closes smoothly (that is, without a cusp) can be reasonably described by a parabolic form. To substantiate the theory, we now consider the energy flux through a contour C_{nl}, taken well within the nonlinear zone, at a scale of a few tens of micrometers. In this region, the asymptotic solution in Eq. 2, when used in Eq. 1, yields an expression for the asymptotic neo-Hookean energy flux G_{nl}

$$G_{nl}(v) = \mu a^2(v) \int_{-\pi}^{\pi} I(\theta; v)\, d\theta \qquad (3)$$

where the function $I(\theta;v)$ is provided in (*24*).

At $r < 200$ μm, we are generally unable to measure particle displacements because of the extreme strains and lensing effects in this region. We therefore use extrapolated values of $b(v)$ to extract $a(v)$ from the data of Fig. 3B and calculate G_{nl} in Eq. 3. G_{nl} is compared with G measured at the outer-millimeter scales in Fig. 2B. The values of G_{nl} and G agree to well within our uncertainty in $b(v)$ and thereby provide direct validation of both the solution in Eq. 2 and our interpretation of the small-scale crack-tip profile. Furthermore, because no dissipation is observed within the nonlinear zone, we conclude that dissipation is

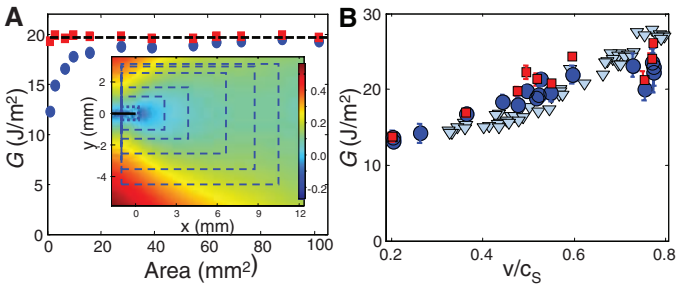

Fig. 2. (**A**) The energy flux G is computed over different contours using Eq. 1 for both the neo-Hookean (red squares) and linear elastic (blue circles) constitutive laws. (Inset) The measured displacement field u_x of the crack shown in Fig. 1B (color bar in millimeters). Dashed blue rectangles mark every second contour used for calculating G. The results are independent of the contour symmetry about the crack (denoted by the black line with its tip at the origin). (**B**) A comparison of G as a function of v, derived at different distinct regions using very different machineries: red squares, G derived using Eq. 1 for a neo-Hookean stress-strain relation; blue circles, G derived according to the weakly nonlinear theory (*5*) using the millimeter-scale parabolic crack-tip opening displacement [curvature data taken from (*28*)]; light blue triangles, G_{nl} derived from the small-scale curvature and estimated values of b (defined in Eq. 2) using the large deformation theory of Eq. 3.

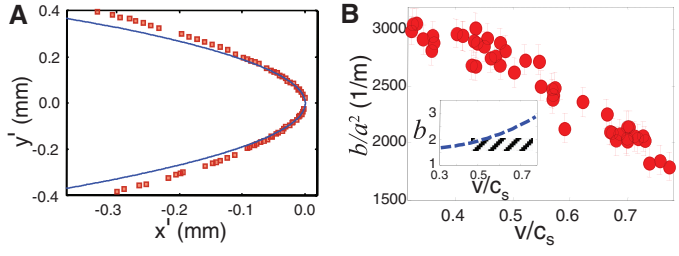

Fig. 3. The material deformation adjacent to the dissipative zone is quantitatively described by the large deformation theory. (**A**) Within ~40 μm from the crack tip (here, moving at $v = 0.43c_S$), the measured crack-tip profile (squares) corresponds to the parabolic form predicted by Eq. 2. The near-tip parabolic form of the crack-tip profile differs from that predicted by LEFM, which properly describes the measured profile at large scales. (**B**) The crack-tip curvature b/a^2 as a function of v. Independent measurements of a and b in the near-tip region, however, are hampered by lensing effects as seen in Fig. 1B (left). In the large-deformation region, $\partial_x u_x = (b - 1)$ along the crack propagation direction ($\theta = 0$). (Inset) An estimate of b (dashed blue curve) by extrapolating the $\partial_x u_x(v)$ measurements on this axis at $r = 200$ μm (typical measurement limit) by assuming a $1/r$ increase down to the typical outer scale, $r = 40$ μm, of the large-deformation region. This $1/r$ strain growth is predicted by the weakly nonlinear theory (*5*) and should become more dominant as the crack tip is approached. For comparison, the shaded region denotes values of b estimated from discrete $\partial_x u_x$ measurements at scales of $r = 120$ to 170 μm.

confined to a region that is smaller than our minimal observation scale (~20 μm).

These measurements provide experimental validation of both the existence of the asymptotic solution (Eq. 2) and the scales at which it is relevant. There is a long-standing conundrum in fracture mechanics that is solved by the existence of this solution. LEFM predicts that $\partial_x u_x$ is larger than $\partial_y u_y$ ahead of the crack tip. Because one would intuitively expect that the bonds that are most deformed would fail first, this implies that fracture should occur in the orthogonal direction (y) to the observed propagation direction (x). Equation 2 solves this problem [as first noted in (*31*)] if this asymptotic solution is indeed realized. Our measurements now demonstrate this explicitly under fully dynamic conditions; indeed, $\partial_y u_y$ is greater than $\partial_x u_x$ at the near-tip scales $r < 30$ to 40 μm. This example demonstrates how the structure of the highly nonlinear region near the crack tip may be critical in determining a crack's path.

With the validity of Eq. 2 established, we can combine this small-scale solution with the weakly nonlinear solution (*5*) to construct both the overall shape of the crack tip and $\delta(v)$. An estimate of the crack-tip location is obtained by extrapolating the weakly nonlinear solution (*5*, *30*) to the strongly nonlinear zone until it closes. Although it is beyond the theory's formal range of validity, this estimate yields values of $\delta(v)$ that agree well (see Fig. 4B) with measured values over the entire range of v. The scale of $\delta(v)$ is an intrinsic one and is determined by the ratio of the linear and quadratic terms in the stress-strain relation of a given material. For neo-Hookean materials, $\delta(v) \sim G/\mu$.

The crack-tip profile is then obtained from Eq. 2 by plotting the small-scale parabolic crack-tip profile [using measured values of either $b(v)/a^2(v)$ or G and $b(v)$] from the estimated crack-tip location until it intersects the weakly nonlinear solution. Concatenating these solutions yields profiles (for example, Fig. 4A) that are in excellent agreement with the measured ones. Surprisingly, even in the strongly nonlinear zone, the form of the divergences from a parabolic form of the crack-tip profile is reasonably captured by the logarithmic corrections to the displacement fields that are predicted by the weakly nonlinear theory (*5*, *30*), which justifies the only assumption made in this approach. The weakly nonlinear solution is uniquely defined once G and the constitutive law are known.

We have shown that linear elasticity, which provides a good description at large scales (Fig. 4C, left), must be supplemented by a fully nonlinear elastic description as the crack tip is approached (Fig. 4C, right). These nonlinear fields form the bridge to scales where irreversible deformation and fracture are really taking place ($r <$ 20 μm in our system).

This work describes a combined experimental and analytic description of the nonlinear elastic region that links LEFM to scales bordering dissipative scales. This quantitative description of the elastic fields surrounding a single straight crack has been demonstrated here for a specific class of materials. We expect, however, that the same qualitative picture holds true for any brittle material. In the near-tip vicinity where extreme strains prevail, linear elasticity cannot be expected to give a correct description of a material's elastic response. Addressing the nonlinear elastic response near the crack tip extends LEFM to the small scales where fracture takes place. Nonlinearity of elastic fields must occur in the region of high strains that is generated near a crack's tip in any material undergoing fracture, even in materials that macroscopically appear to be ideally brittle, although the complete separation of the nonlinear elastic region from the dissipative zone as shown here may not, necessarily, be general.

The existence of this nonlinear elastic region may hold the key to resolving many previously intractable puzzles in fracture mechanics. The correct description of the fields in this region has already presented concrete solutions to open problems related to dynamic crack path selection. Other open problems, such as LEFM's failure to predict how the straight single-crack states studied here become unstable at high velocities (*4*, *27*), may now be resolvable in this framework (*36*). Two possibilities exist: Either the instabilities are critically dependent on the dissipative mechanisms that were not considered here or they are due to the elastic fields surrounding the dissipative zone (*11*). Identical crack-tip instabilities have been observed in materials with wholly different dissipative mechanisms (*27*); therefore, we view the latter possibility as likely, although the former cannot be entirely ruled out.

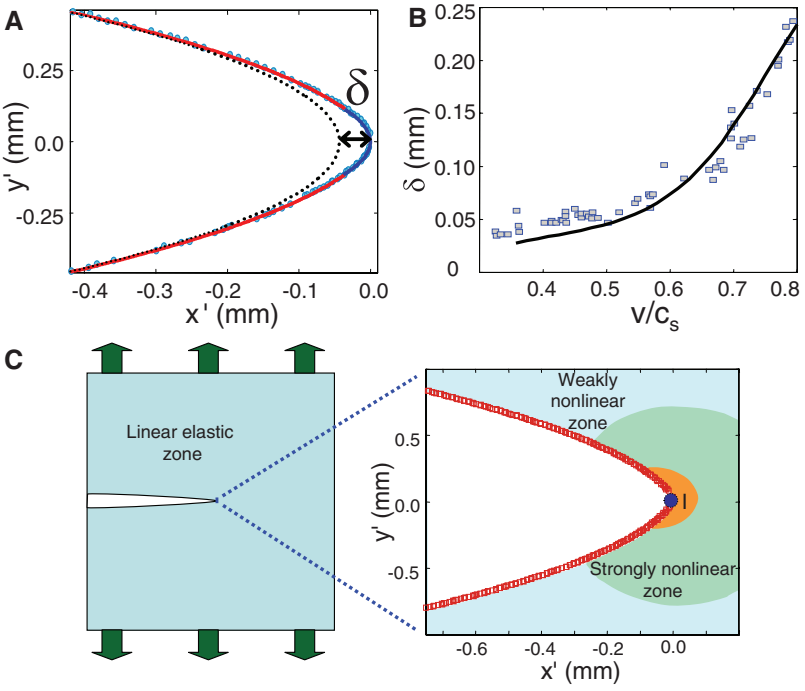

Fig. 4. Addressing the different elastic zones in the vicinity of a crack tip provides a full description of the material deformation down to the dissipation scales. (**A**) The circles indicate the measured crack-tip profile of Fig. 3A, compared to concatenation of the predicted profiles of the (red line) weakly nonlinear (*5*) and (blue line) asymptotic (see Eq. 2) theories. The dotted line is the LEFM solution. (**B**) Comparison of measured values (squares) of $\delta(v)$ with the estimated values (line) obtained by extrapolating the weakly nonlinear solution (*5*, *30*) to the strongly nonlinear zone until it closes. (**C**) A schematic sketch of the different elastic regions surrounding a crack. Energy and stresses are transmitted from the large scales, where material deformation is described by linear elasticity (left), through a hierarchy of nonlinear elastic regions (right) until dissipated by plastic deformation and fracture at the smallest scales (circle). The asymptotic region, denoted by *I*, is where strains become larger than unity and Eq. 2 is valid. Shown (squares) are measurements of the crack-tip profile extracted from Fig. 1A (right).

References and Notes

1. L. B. Freund, *Dynamic Fracture Mechanics* (Cambridge Univ. Press, New York, 1990).
2. E. Sharon, J. Fineberg, *Nature* **397**, 333 (1999).
3. J. Fineberg, M. Marder, *Phys. Rep.* **313**, 1 (1999).
4. A. Livne, O. Ben-David, J. Fineberg, *Phys. Rev. Lett.* **98**, 124301 (2007).
5. E. Bouchbinder, A. Livne, J. Fineberg, *Phys. Rev. Lett.* **101**, 264302 (2008).
6. T. Baumberger, O. Ronsin, *Eur. Phys. J. E*, **31**, 51 (2010).
7. F. F. Abraham, D. Brodbeck, R. A. Rafey, W. E. Rudge, *Phys. Rev. Lett.* **73**, 272 (1994).
8. D. Holland, M. Marder, *Phys. Rev. Lett.* **80**, 746 (1998).
9. P. Gumbsch, R. M. Cannon, *MRS Bull.* **25**, 15 (2000).
10. J. S. Langer, *Phys. Rev. E Stat. Phys. Plasmas Fluids Relat. Interdiscip. Topics* **62**, 1351 (2000).
11. M. J. Buehler, H. J. Gao, *Nature* **439**, 307 (2006).
12. E. Bouchbinder, A. Pomyalov, I. Procaccia, *Phys. Rev. Lett.* **97**, 134301 (2006).
13. M. L. Falk, A. Needleman, J. R. Rice, *J. Phys. IV* **11**, 43 (2001).
14. A. E. Lobkovsky, J. S. Langer, *Phys. Rev. E Stat. Phys. Plasmas Fluids Relat. Interdiscip. Topics* **58**, 1568 (1998).
15. O. Miller, L. B. Freund, A. Needleman, *Model. Simul. Mater. Sci. Eng.* **7**, 573 (1999).
16. M. J. Buehler, F. F. Abraham, H. J. Gao, *Nature* **426**, 141 (2003).

17. H. J. Gao, *J. Mech. Phys. Solids* **44**, 1453 (1996).
18. E. Bouchbinder, T. S. Lo, *Phys. Rev. E Stat. Nonlin. Soft Matter Phys.* **78**, 026119 (2008).
19. E. Bouchbinder, J. Mathiesen, I. Procaccia, *Phys. Rev. Lett.* **92**, 245505 (2004).
20. K. Ravi-Chandar, B. Yang, *J. Mech. Phys. Solids* **45**, 535 (1997).
21. T. Pardoen, J. W. Hutchinson, *J. Mech. Phys. Solids* **48**, 2467 (2000).
22. I. S. Aranson, V. A. Kalatsky, V. M. Vinokur, *Phys. Rev. Lett.* **85**, 118 (2000).
23. A. Karma, D. A. Kessler, H. Levine, *Phys. Rev. Lett.* **87**, 045501 (2001).
24. See supporting material on *Science* Online.
25. R. S. Rivlin, *Philos. Trans. R. Soc. Lond. Ser. A* **240**, 459 (1948).
26. L. R. G. Treloar, *The Physics of Rubber Elasticity* (Oxford Univ. Press, New York, 1975).
27. A. Livne, G. Cohen, J. Fineberg, *Phys. Rev. Lett.* **94**, 224301 (2005).
28. A. Livne, E. Bouchbinder, J. Fineberg, *Phys. Rev. Lett.* **101**, 264301 (2008).
29. J. K. Knowles, E. Sternberg, *J. Elast.* **13**, 257 (1983).
30. E. Bouchbinder, A. Livne, J. Fineberg, *J. Mech. Phys. Solids* **57**, 1568 (2009).
31. J. K. Knowles, E. Sternberg, *J. Elast.* **3**, 67 (1973).
32. J. K. Knowles, A. J. Rosakis, *J. Appl. Mech.* **53**, 545 (1986).
33. A. M. Tarantino, *J. Elast.* **57**, 85 (1999).
34. M. Marder, *J. Mech. Phys. Solids* **54**, 491 (2006).
35. V. R. Krishnan, C. Y. Hui, R. Long, *Langmuir* **24**, 14245 (2008).
36. E. Bouchbinder, *Phys. Rev. Lett.* **103**, 164301 (2009).
37. This research was supported by grant 57/07 of the Israel Science Foundation. J.F. acknowledges the support of the Max Born Chair for Natural Philosophy.

Supporting Online Material

www.sciencemag.org/cgi/content/full/327/5971/1359/DC1
Materials and Methods
References

12 August 2009; accepted 22 January 2010
10.1126/science.1180476

Imaging Local Electrochemical Current via Surface Plasmon Resonance

Xiaonan Shan,[1,2] Urmez Patel,[1] Shaopeng Wang,[1] Rodrigo Iglesias,[1] Nongjian Tao[1,2]*

We demonstrated an electrochemical microscopy technique based on the detection of variations in local electrochemical current from optical signals arising from surface plasmon resonance. It enables local electrochemical measurements (such as voltammetry and amperometry) with high spatial resolution and sensitivity, because the signal varies with current density rather than current. The imaging technique is noninvasive, scanning-free, and fast, and it constitutes a powerful tool for studying heterogeneous surface reactions and for analyzing trace chemicals.

Electrochemical detection is a powerful analytical method that has been used for a wide range of applications, including trace chemical analysis, glucose and neurotransmitter monitoring, DNA and protein detections, and electrocatalysis studies. Measurement of the total electrochemical current or other related electrical quantities of an electrode cannot directly provide local reaction information from the electrode surface, which is required for analyses of heterogeneous reactions, local activities of cells, and protein and DNA microarrays. Scanning electrochemical microscopy (SECM) (*1*), which probes local electrochemical current by scanning a microelectrode across the surface, can overcome this limitation and has found numerous applications (*2*). However, the sequential scanning of the microelectrode limits its speed, and the scanning probe may perturb the local electrochemical processes under study. The current measured by the microelectrode in SECM scales with the size of the microelectrode, making it increasingly difficult to improve the spatial resolution by shrinking the microelectrode.

Here, we report a method for imaging local electrochemical current without the use of a scanning probe or a microelectrode. Instead of measuring the current with an electrode, it determines the electrochemical current density from an optical signal of the electrode surface generated from a surface plasmon resonance (SPR) (*3*, *4*). Important benefits of this approach include fast and noninvasive electrochemical current imaging of the surface. In addition, the measured local current signal is proportional to the optical signal, which does not scale with the area of a region of interest. We imaged local electrochemical currents generated by heterogeneous surface reactions, and we could perform the traditional electrochemical detection methods—such as amperometry, cyclic voltammetry, and square-wave voltammetry—locally, interrogating areas as small as 0.2 μm by 3 μm with a current sensitivity of 0.3 pA. We also demonstrate sensitive and selective trace analysis with the technique.

An electrochemical reaction taking place on an electrode always involves electron transfer between the electrode and the reactant, which is measured as an electrochemical current or related electrical signal in the conventional electrochemical methods. The electron transfer process is always accompanied by a conversion of chemical species between oxidized and reduced states, so the electrochemical current can be determined by monitoring the conversion of the chemical species on the surface, which is the principle of the present imaging technique. Relative to other optical detection methods such as phase-measurement microscopy (*5*) that have been used to study local molecular binding events and electrochemical reactions on surfaces (*6*, *7*), SPR is extremely sensitive to the species generated (or consumed) on the electrode surface (Fig. 1A). We show that the concentration of the species is directly related to the electrochemical current via Fick's law of diffusion (*8*); more important, the electrochemical current density $i(t)$ can be easily calculated from the local SPR signal according to

$$i(t) = bnFL^{-1}[s^{1/2}\Delta\tilde{\theta}_{SPR}(s)] \quad (1)$$

(*9*), where $b = [B(\alpha_R D_R^{-1/2} - \alpha_O D_O^{-1/2})]$, n is the number of electrons involved in the redox reaction, F is the Faraday constant, L^{-1} is the inverse Laplace transform, and $\Delta\tilde{\theta}_{SPR}(s)$ is the Laplace transform of the SPR signal. In the expression for b, α_O and α_R are the changes in the local refractive indices per unit concentration for the oxidized and reduced molecules, D_O and D_R are the diffusion coefficients of the oxidized and reduced molecules, and B measures the sensitivity of the SPR signal to a change in the bulk index of refraction, which can be calibrated independently. According to Eq. 1, the measured signal, $i(t)$, does not scale with the image area, which is in contrast to the conventional electrochemical detection methods. Note that double layer charging current also contributes to the SPR signal (*10*), which is, however, small (*11*) relative to faradaic current.

We show below that (i) the electrochemical current determined using Eq. 1 is indeed equivalent to that obtained from the conventional electrochemical methods; (ii) the new electrochemical imaging technique provides local electrochemical current (e.g., cyclic voltammograms) associated with heterogeneous surface reactions; (iii) the advantages of this imaging technique allow for sensitive and selective trace analysis; and (iv) the technique offers high current sensitivity, a fast imaging rate, and good spatial resolution.

Two optical configurations were used in the experiments. In the first configuration, the working electrode was an Au-coated glass slide attached onto a prism via index-matching fluid. An electrochemical cell made from Teflon was mounted on top of the Au electrode. A Pt wire counterelectrode and an $Ag|AgCl|KCl_{(sat.)}$ reference electrode, together with a potentiostat, were used to control the potential of the working electrode. A light-emitting diode (LED) with a peak wavelength of 670 nm was used to excite the surface plasmons in the Au electrode, and a charge-coupled device (CCD) camera was used to record the image. Calculating the current at each pixel from the image by means of Eq. 1 creates an elec-

[1]Center for Bioelectronics and Biosensors, Biodesign Institute, Arizona State University, Tempe, AZ 85287, USA. [2]Department of Electrical Engineering, Arizona State University, Tempe, AZ 85287, USA.

*To whom correspondence should be addressed. E-mail: njtao@asu.edu